Applied Catalysis B: Environmental 231 (2018) 277–282

Contents lists available at ScienceDirect

Applied Catalysis B: Environmental

journal homepage: www.elsevier.com/locate/apcatb

Seed-mediated synthesis of large-diameter ternary TePtCo nanotubes for enhanced oxygen reduction reaction

Wenqiang Li[a,1], Yuli Xiong[b,1], Zhe Wang[a], Mingjun Bao[a], Jing Liu[a], Daping He[a,c,**], Shichun Mu[a,*]

[a] State Key Laboratory of Advanced Technology for Materials Synthesis and Processing, Wuhan University of Technology, Wuhan, 430070, China
[b] Wuhan National Laboratory for Optoelectronics, School of Optical and Electronic Information, Huazhong University of Science and Technology, Wuhan, China
[c] Hubei Engineering Research Center of RF-Microwave Technology and Application, Wuhan University of Technology, Wuhan, 430070, China

ARTICLE INFO

Keywords:
TePtCo alloy
Nanotubes
Oxygen reduction reaction (ORR)
Electrocatalyst
DFT calculation

ABSTRACT

Compared to Pt nanoparticles, Pt metal nanotubes (NTs) with hollow nanostructures and ultrathin side walls can greatly increase electrocatalytic activity and stability in oxygen reduction reaction (ORR). In this work, the large-diameter ternary TePtCo NT with a hollow and hierarchical structure is successfully prepared by a simple and cost-effective replacement way. The formed TePtCo NT not only proves the high Pt utilization with large surface area, but also improves the proton transfer in the ORR process. As expected, its specific activity and mass activity at 0.9 V (vs. RHE) are 4.6 folds and 3.9 folds over that of the commercial Pt/C catalyst, respectively. Moreover, it also shows an excellent catalytic stability, much higher than that of Pt/C. The density functional theory (DFT) calculation results reveal that Pt alloying with Te and Co facilitates the breakage of the O—O bond and weakens the adsorption energy of hydroxyl, subsequently enhancing the ORR performance.

1. Introduction

As an efficient oxygen reduction reaction (ORR) catalyst, noble metal platinum (Pt) nanoparticle (NP) catalysts have been developed for decades [1,2]. However, owning to the high dosage and low stability of commercial Pt NP catalysts under harsh operating conditions, it is an urgent need to design a new and highly efficient Pt-based electrocatalyst with greatly improved activity and stability [3–5]. As reported, the chemical properties of metal nanostructures can be optimization by controlling their form, size, and crystallinity [6,7]. Hitherto, to enhance the catalytic performance, many methods have been exploited to manufacture Pt nanostructures with different morphologies [8–11]. Especially, for one-dimensional (1D) nanostructures, the interaction between crystal facets and oxygenated species as well as the carbon support can be rationally designed to comply high catalytic activity and stability [12–14]. Among 1D nanostructures, Pt based hollow metallic nanotubes (NTs) are of particular interest due to their unique tubular feature which can improve the mass transport and catalyst utilization [15]. Compared to the commercial Pt/C catalysts, Pt-based NTs expose specific crystal face and optical electronic structure of the surface Pt atoms, beneficial to improve ORR performance. Moreover, Pt-based NTs also show a durability under potential cycling conditions due to importantly reducing aggregation, dissolution and ripening of Pt [16–21].

Compared to binary Pt-M alloys, ternary Pt-based alloys by incorporating of the extra metal can further reduce the total cost of catalysts by decreasing the amount of Pt, and meanwhile exhibit better catalytic activity through a favorable synergistic electronic interaction between Pt active sites and transition metal dopants [22–24]. Moreover, Sun and Wong et al. demonstrated that, by introducing a third transition metal (Fe), the activity of PtM (M = Ru, Pd) was enhanced due to improved availability of active sites [25,26]. Recently, as the template-directed replacement reaction is a simple and cost-effective method to prepare NTs, Pt-based alloy NTs have also been developed by this solution [27,28].

Taken together, alloying and structuring are two promising approaches to developing efficient and durable electrocatalysts for ORR. The Pt-based alloy NT represents an ideal model to combine both of them. In this work, we present large diameter ternary TePtCo NTs through the template-directed replacement reaction, and further investigate their ORR catalysis nature in a 0.1 M $HClO_4$ solution. The novel TePtCo alloy shows exclusive higher catalytic activity and durability compared with the commercial Pt/C catalyst. To further probe the catalytic mechanism of TePtCo NTs, the density functional theory

* Corresponding author.
** Corresponding author at: State Key Laboratory of Advanced Technology for Materials Synthesis and Processing, Wuhan University of Technology, Wuhan, 430070, China.
E-mail addresses: hedaping@whut.edu.cn (D. He), msc@whut.edu.cn (S. Mu).
[1] These authors contributed equally to this work.

https://doi.org/10.1016/j.apcatb.2018.03.022
Received 29 November 2017; Received in revised form 31 January 2018; Accepted 7 March 2018
Available online 08 March 2018
0926-3373/

(DFT) calculation is carried out.

2. Materials and methods

2.1. Synthesis of TePtCo nanotubes

6.4 mg Te NW (The preparation process of Te NW can be seen in Support information) was dissolved in 20 ml ethylene glycol. After ultrasound for half hour, the solution was transferred into a round flask. Then, 13 ml $H_2PtCl_6{\cdot}6H_2O$ solution (1.5 mg_{Pt}/ml) was slowly injected into the prepared solution. After mixing at 50 °C for 2 h and rising temperature to 180 °C, 15.2 mg $CoCl_2{\cdot}6H_2O$ was slowly pour into. Then the mixed-solution was further stirred at 180 °C for 5 h. At last, the sample was cooled to room temperature. The final precipitate was collected by filtration, washed with distilled water and ethanol, and dried at a vacuum atmosphere. TePt NTs as benchmark were achieved by absence of $CoCl_2{\cdot}6H_2O$, while keeping the other parameters the same to the preparation of TePtCo NTs.

2.2. Synthesis of TePtCo NTs/C catalysts

5 mg TePtCo NTs, TePt NTs and 10 mg XC-72 were dispersed in a certain amount of ethanol, mixed and ultrasound for around 2 h. The product was collected by filtration, washed with DI water for several times, and dried at 60 °C under vacuum. The related material characterization and equipment are present in Support information.

2.3. Electrochemical measurements

The electrochemical properties of catalysts were investigated by a three-electrochemical cell using the CHI 660E. The saturated calomel electrode (SCE) was used as the reference electrode, and the platinum wire was used as the counter electrode. But all the SCE electrode potential were converted to reversible hydrogen electrode (RHE) by $E_{vs.RHE} = E_{.SCE} + 0.305V$ by calibration (Fig. S1). A certain amount of catalyst powder was mixed with 100 µl deionized water, 900 ul isopropyl alcohol and 20 µl 5 wt% Nafion solution. And then, a certain amount of catalyst suspension was coated on the glassy carbon electrode (diameter: 5 mm, area: 0.196 cm^2) for electrochemical tests. The Pt loading of TePtCo NTs/C, TePt NTs /C and Pt/C was 19.2, 19.55 and 20 µg/cm^2, respectively.

All measurements were carried out in 0.1 M $HClO_4$ solution. The working electrodes were first electrochemically cleaned via potential cycling for 100 cycles at 100 mV/s between 0 and 1.20 V versus the RHE before measuring the Oxygen reduction reaction (ORR). ORR measurements were conducted in the 0.1 M $HClO_4$ solution which was purged with oxygen during the measurement. The scan rate for ORR measurements was 50 mV/s. The ORR polarization curves were collected at 1600 rpm. The accelerated durability tests (ADT) were performed at room temperature in O_2-staturated 0.1M $HClO_4$ solutions by applying cyclic potential sweeps between 0.6 and 1.0 V versus Reversible Hydrogen Electrode (vs. RHE) at a sweep rate of 100 mv/s for 10,000 cycles.

3. Results

3.1. Synthesis and characterization of TePtCo NTs

As shown in Fig. 1, the synthesis of TePtCo NTs involves three steps: First, large diameter Te nanowires (NWs) as the precursor for TePtCo NTs, are prepared. And then the formed Te nanowires are used as the sacrificial template for fabrication of the Pt-skin NTs catalysts through replacement between Te nanowires and Pt precursors at 50 °C for 2 h. Lastly, by keeping temperature at 180 °C for 5 h, Co elements in precursors are further reduced by ethylene glycol to form TePtCo NTs [29,30]. According to the ICP measurement, the atomic ratio of Te, Pt and Co is 40:53:7. The formation mechanism for TePtCo nanotubes relies on the stoichiometric relationship shown in Eqs. (1) and (2).

$$PtCl_6^{2-} + Te + 2H_2O \rightarrow Pt + TeO_2 + 4H^+ + 6Cl^- \quad (1)$$

$$PtCl_6^{2-} + Te + Co^{2+} + 2(CH_2OH)_2 + 3H_2O \xrightarrow{180°C} TePtCo + 3CO_2 + CO + 6H^+ + 6Cl^- + 6H_2 \quad (2)$$

The Kirkendall effectt can be used to illustrate the growth mechanism of hollow structures [31]. The substitution reaction between Te atoms and $PtCl_6^{-1}$ creates many defects. The formed defects on the nanowires favor the transport speed of the internal Te atoms to the surface, and meanwhile slowdown the reduction speed of external Pt atoms, leading to the formation of voids [32]. Subsequently, these voids tend to grow and collapse in the center, until the interior material disappears, eventually leaving alloy NTs behind [33].

Fig. S2 shows the typical SEM and TEM image of Te nanowires and TePtCo NTs. Te nanowires (Fig. S2A) and TePtCo NTs (Fig. S2B) present large diameter distribution with length up to several micrometers. Many NPs appear on the surface of Te nanowires, forming the alloy nanotubes. Interestingly, the open-end and hollow structure at the top of wire-like TePtCo is highlighted in Figs. S2C and S2D, proving the existence of hollow interior in TePtCo NTs.

To further identify the structure and composition of TePtCo NTs, STEM and HRTEM observations were performed. From Fig. 2A, it can be seen that the average diameter and wall thickness of hollow alloy nanotubes are about 140 and 50 nm, respectively. HRTEM images (Fig. 2B) further reveal that small NPs with a size of around 10 nm consist of NTs. The clear lattice fringes of NPs with an interplanar distance of approximately 0.22 nm, correspond to the (111) plane of the face-centered cubic (fcc) alloy structure. The contrast between the edge and middle of the NTs under HAADF-TEM (Fig. 2C) indicates a typical hollow feature for the tubular nanostructure. To investigate the distribution of Te, Pt, and Co elements, the elemental mapping was carried out by HAADF-STEM-EDS (Fig. 2C). It can be seen that Te, Pt, and Co elements are evenly distributed throughout the whole tube wall, demonstrating that the composition of as-prepared NTs consist of ternary TePtCo alloys. The typical double peaks in the elemental line scan along the radial direction further confirm that TePtCo NT has a nature of tubular structures. (Fig. 2D).

Fig. S3A shows XRD patterns of Pt/C, TePt NTs/C and TePtCo NTs/C. Three peaks at 39.9°, 46.2°, and 67.4° can be assigned to the (111), (200), and (220) planes of fcc structure, respectively, while the other peaks located at 30.6°and 45.5° are assigned to the(111) and (210) plane of PtTe. Since the atomic size of Te is larger than that of Pt, a negative shift of the (111) plane occurs in binary TePt NT compared to that of Pt/C. However, after Co atoms were introduced into TePt NT, the peak of TePtCo shifts up (Fig. S3B).This result indicates the contraction of lattices occurs by incorporation of Co in the TePt NTs during the alloying process [34,35].

The chemical state of Pt in TePtCo NTs/C, TePt NTs/C, Pt/C was probed by XPS as shown in Fig. S4. The Pt 4f spectrum of TePtCo NTs, TePt NTs, Pt/C could be fitted into two pairs of doublets (Fig. S4). Table S1 summarizes the results of peak deconvolution. For TePtCo NTs/C, the most intense doublet at 71.87 and 75.17 eV is raised from metallic Pt (0), while the second and weaker doublet at 72.87 and 76.17 could be assigned to the Pt(II) states in PtO and $Pt(OH)_2$ [4,36]. The high ratio for Pt(0)/Pt(II) implies that the zero-valent state of Pt is predominant in the samples. Significantly, the binding energy of the Pt(0) state core-levels for TePtCo has a negative shift in comparison with that of pure Pt and TePt/C (Fig. S3 and Table S1) due to the decreased 5d electron in Pt-based alloy systems. This result indicates TePtCo NTs have lower chemical adsorption of OH_{ads} on the alloy surface, facilitating the ORR activity of catalyst [37–41]. In addition, the Co 2p3/2 signal also appears in TePtCo NTs, proving the existence of the ternary alloy. (Fig. S4D).

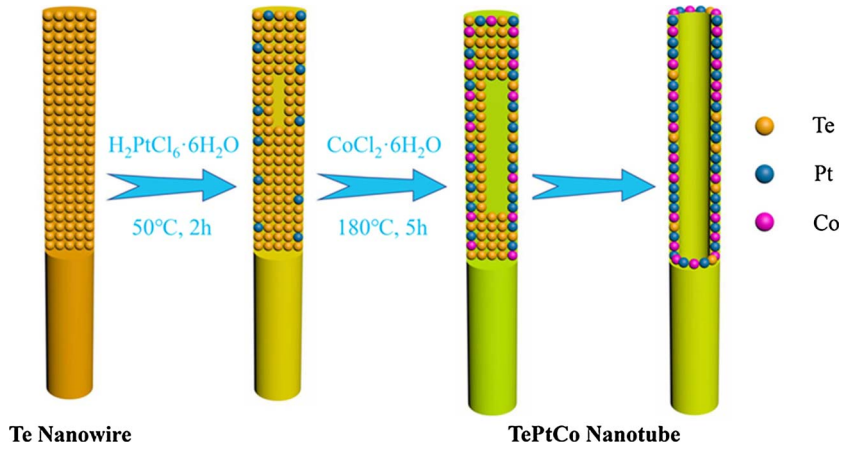

Fig. 1. Schematic illustration of the formation process for ternary TePtCo nanotube.

3.2. Electrochemical performance of TePtCo NTs

To examine the electrochemical performance of TePt NTs/C, TePtCo NTs/C and Pt/C catalysts in acid media, Cyclic Voltammetry (CV) was carried out. Fig. 3A shows the CV curves in a 0.1M $HClO_4$ solution. The electrochemical surface area (ECSA) of TePtCo NTs/C and TePt NTs /C is 60.1 and 40.6 m^2/g, respectively.

ORR polarization curves of TePtCo NTs/C, TePt NTs/C and Pt/C catalysts are shown in Fig. 3B. TePtCo NTs/C displays a higher ORR onset potential than that of Pt/C (0.98 V) and TePt NTs /C (0.982 V) at 1.01 V (vs.RHE). The half-wave potentials for TePtCo NTs/C and TePt NTs/C are 0.924 V and 0.907V, respectively. Compared with Pt/C (0.878 V), it presents 46 mV and 29 mV positive shifts, respectively. To evaluate the intrinsic ORR activity of catalysts, the mass activity and the specific activity of catalysts at 0.9 V (vs. RHE) were compared. TePtCo NTs/C exhibits an remarkbale mass activity of 0.7 A/mg_{Pt} at 0.9V, about 3.9 times and 1.6 times higher than that of Pt/C(0.18 $A/mg_{Pt)}$ and the target (0.44 A/mg_{Pt}) of 2020 for U.S. Department of

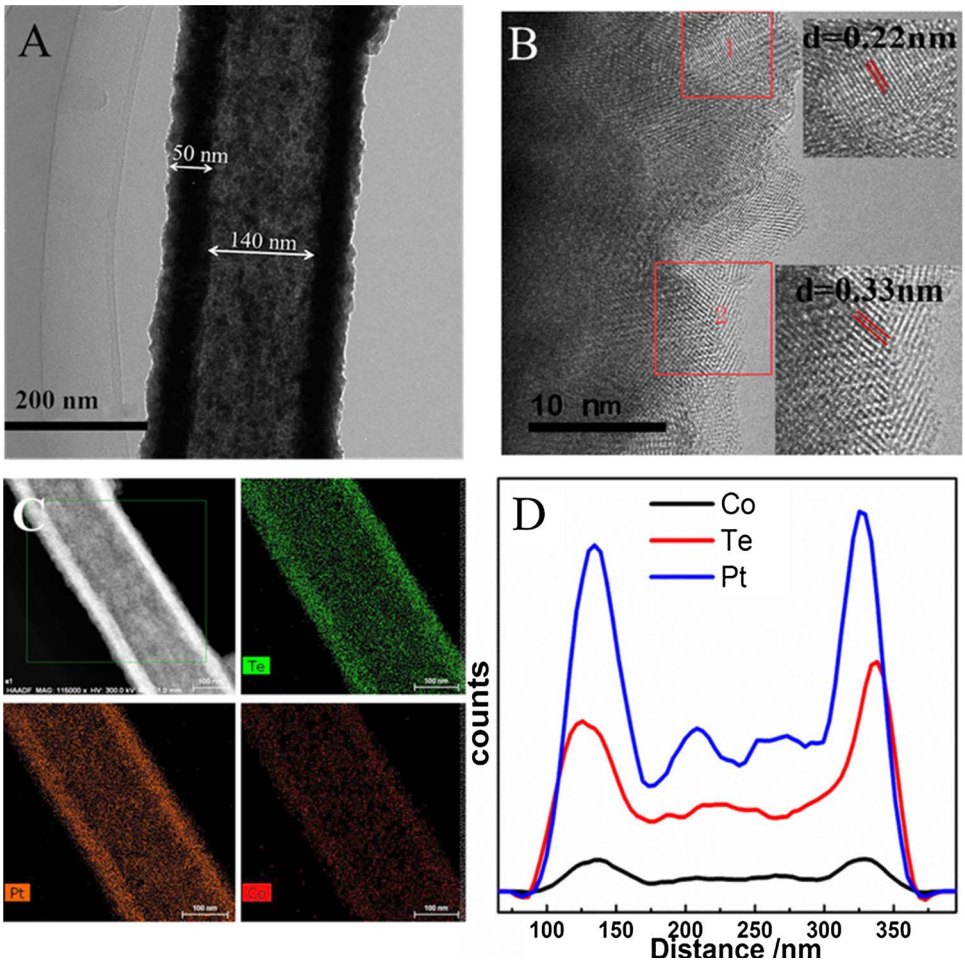

Fig. 2. Morphology and microstructure of TePtCo NTs. (A) TEM image of an individual TePtCo NT, (B) HRTEM images of the edge walls of ternary TePtCo NT. The inset in (b) are the enlarged image taken from the square area marked as 1, 2. (C) HAADF-STEM and HAADF-STEM-EDS element mapping images of Te, Pt, Co elements in ternary TePtCo NT. (D) EDX line-scanning profile of TePtCo NT.

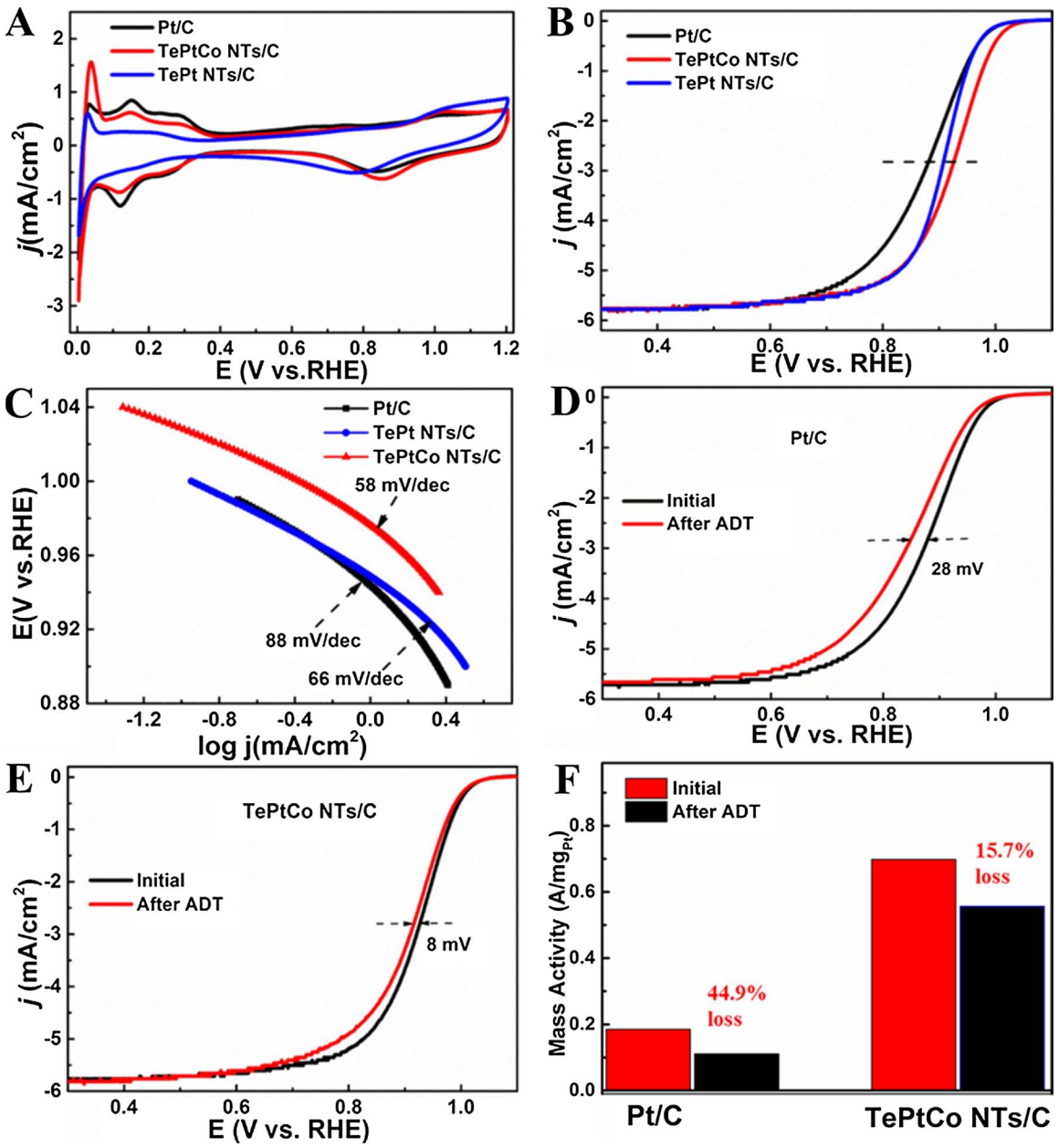

Fig. 3. (A) CV profiles of TePtCo NTs/C, TePt NTs/C and Pt/C catalysts in N_2 saturated 0.1 M $HClO_4$ (sweep rate: 50 mV/s). (B) LSVs of TePtCo NTs/C, TePt NTs/C and Pt/C catalysts in O_2-saturated in 0.1 M $HClO_4$ (sweep rate: 5 mV/s, 1600 rpm). (C) Corresponding Tafel curves Pt/C and TePt NTs/C and TePtCo NTs/C. (D) and (E) ORR polarization curves the Pt/C and TePtCo NTs/C after 10,000 cycles, (F) mass activities of the Pt/C and TePtCo NTs/C after 10,000 cycles for ORR at 0.9 V vs.

Energy, respectively [42]. Moreover, TePtCo NTs/C presents the specific activity of 1.15 mA/cm^2 which is about 4.7 times higher than that of Pt/C (0.245 mA/cm^2). As displayed in Fig. 3C, the Tafel slope (58 mV/dec) of TePtCo NTs/C is much lower than that of Pt/C (88 mV/dec), and slightly lower than that of TePt NTs/c (66 mV/dec), suggesting that TePtCo NTs/C possesses much faster electron transfer rate and superior ORR activity compared to Pt/C

For the mechanism of the dramatically improved activity, two main aspects are proposed: 1) The unique tubular structure allows the existence of some extended Pt surfaces with intrinsically high ORR specific activities on the side walls, leading to dramatically enhanced overall ORR performance. 2) The larger diameter NTs with open and hollow structures facilitate the reaction kinetics and electron transport, as well as improve the diffusion of O_2 to Pt surface [28,36].

Accelerated durability test (ADT) was adopted to assess the stability of catalysts. The changes in ORR polarization curves of TePtCo NTs/C and Pt/C are shown in Fig. 3D and E. For TePtCo NTs/C, the half-wave potentials of electrode shift to the negative direction for 8 mV, while 28 mV for Pt/C. After the accelerated durability tests, Pt/C exhibits a larger ORR mass activity loss (about 44.9%). By contrast, TePtCo NTs/C only shows a very small loss in mass activity (15.7%) (Fig. 3F). Based on the above results, we can conclude that the durability of TePtCo NTs catalysts is greatly enhanced compared with that of Pt/C.

The mechanism of the greatly enhanced stability is proposed as follows: 1) The unique 1D metal nanotube structure prevents Pt NPs from aggregation, dissolution and detachment from support materials. 2) The small amount of incorporated Co and Te atoms can suppress the dissolution of Pt atoms by preferentially sacrificing Co and Te atoms during the operation condition, improving the catalysis stability [41,43]. To further reveal the mechanism of the stability enhancement, the morphological and structure changes of TePtCo NTs/C after ADT were characterized by TEM. As shown in Fig. S5, after ADT, the NPs are

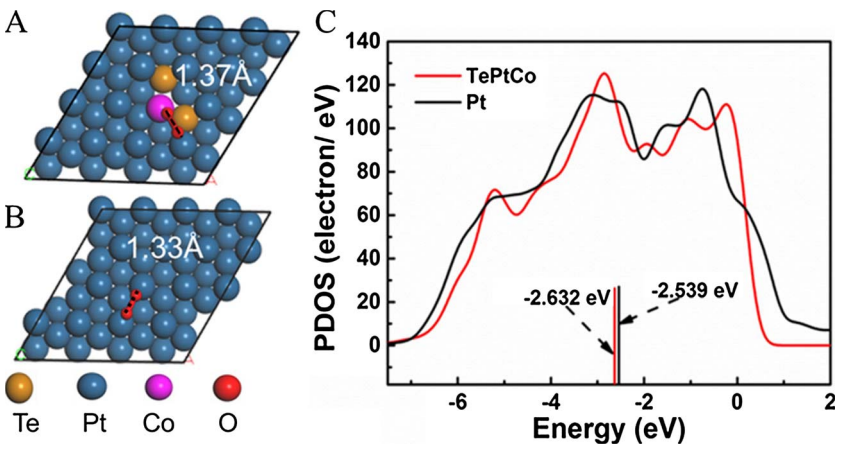

Fig. 4. Model of oxygen adsorbed on (A) TePtCo(111) and (B) Pt (111). (C) PDOS of d orbitals of Pt (111) and TePtCo (111). The calculated d-band centers are marked with lines.

dispersed on NTs are not of aggregation, and no obvious morphology change is shown for TePtCo NTs. This result indicates that the alloying 1D nanotube structure can effectively inhibit the Pt aggregation and greatly improve the stability of catalysts.

3.3. DFT calculations of enhanced catalytic activity for FePtCo nanotubes

In the terms of ORR performance, it can be found that TePtCo NTs have better catalytic activity and stability than Pt/C. To understand the possible mechanism for the improved ORR performance of TePtCo alloy nanotubes, DFT calculations were carried out. According to the model, oxygen can be adsorbed on the Pt-Pt bridge or Co-Pt bridge in the TePtCo(111) slabs. The O_2 adsorption energy (ΔE_{O2}) on the Co-Pt bridge site is 3.14 eV (Fig. 4A), which is higher than that of Pt-Pt bridge (2.52 eV) (Fig. S6). This indicates that O_2 is easily adsorbed on Co-bridge in TePtC (111) slabs compared with Pt–bridge [44]. Meanwhile, the ΔE_{O2} on Pt (111) slabs is 2.33 eV (Fig. 4B), which is smaller than that on TePtCo(111) slabs (3.14 eV), supporting that oxygen molecules are more easily adsorbed on TePtCo (111) slabs than Pt (111) slabs [45]. When oxygen molecules are adsorbed on Pt (111) and TePtCo (111) slabs, the O—O bond (Fig. 4A and B) is stretched to 1.33 Å and 1.37 Å, respectively. As compared with the isolated O_2 molecule (1.237 Å), the obvious change in the O—O bond length mean that the Pt alloying with Te and Co facilitates the damage of the O—O bond [44,46]. In the case of TePtCo NTs, the enhanced O_2 adsorption energy and the weakened O—O bond result in fast scission of the O—O bond, subsequently enhancing the O_2 reduction performance [47,48].

The d band center can be as an independent variable to describe the catalytic activity [49]. As revealed in Fig. 4C, the d-band center of pure Pt (−2.539 eV) (Fig. S7A) shifts down to (−2.632 eV) (Fig. S7B) after alloying with Te and Co. The down-shift of the d-band center of Pt relative to the Fermi level can be attributed to the enhanced strain effect (long-range geometric lattice strain) [50,51]. Such compressive strain decreases the adsorption energy of hydroxyl (ΔE_{OH}) according to the established relationship between the adsorption energy and lattice strain of Pt, [41,45,52,53] resulting in a lower coverage of OH on the surface which has more available active sites for oxygen dissociation [54]. The density functional theory (DFT) calculation results reveal that Pt alloying with Te and Co facilitates the damage of the O—O bond and weakens the adsorption energy of hydroxyl, leading to higher activity compared to Pt/C.

4. Conclusion

In summary, large diameter ternary TePtCo nanotubes (NTs) were successfully synthesized by a simple, cost-effective, aqueous solution method based on the Kirkendall effect. The formed TePtCo NTs showed ultrahigh activity and durability toward ORR. Compared to the commercial Pt/C catalyst, the mass activity was improved by 3.9-folds at 0.9 V. Accelerated durability tests demonstrated that the TePtCo NTs/C catalyst retained 84.3% of its initial activity, much higher than that of Pt/C (55.1%). So, our work provides a promising approach for design of highly active and stable next-generation catalysts with a substantial reduction in Pt amount. As results, the TePtCo NT catalyst is of great potential for use as low-Pt-content ORR catalysts in fuel cells and other applications.

Acknowledgements

We acknowledge support from the National Natural Science Foundation of China (NSFC) through award No. 51672204 and No.51372186. We wish to thank Associate Prof. Xiaoqing Liu and Dr. Tingting Luo for TEM analytical measurements performed at JEM-2100F in the Materials Analysis Center of Wuhan University of Technology.

Appendix A. Supplementary data

Supplementary material related to this article can be found, in the online version, at doi:https://doi.org/10.1016/j.apcatb.2018.03.022.

References

[1] B.C.H. Steele, A. Heinzel, Nature 414 (2001) 345–352.
[2] K.A. Kuttiyiel, K. Sasaki, Y.M. Choi, D. Su, P. Liu, R.R. Adzic, Nano Lett. 12 (2012) 6266–6271.
[3] D. He, S. Mu, M. Pan, Carbon 49 (2011) 82–88.
[4] K. Cheng, Z. Kou, J. Zhang, M. Jiang, H. Wu, L. Hu, X.Y. Yang, M. Pan, S. Mu, J. Mater. Chem. A 3 (2015) 14007–14014.
[5] N. Cheng, M.N. Banis, J. Liu, A. Riese, S. Mu, R. Li, T.K. Sham, X. Sun, Energy Environ. Sci. 8 (2015) 1450–1455.
[6] B. Lim, X. Lu, M. Jiang, P.H.C. Camargo, E.C. Cho, E.P. Lee, Y. Xia, Nano Lett. 8 (2008) 4043–4047.
[7] C. Wang, H. Daimon, Y. Lee, J. Kim, S. Sun, J. Am. Chem. Soc. 129 (2007) 6974–6975.
[8] S.I. Lim, I. Ojea-Jiménez, M. Varon, E. Casals, J. Arbiol, V. Puntes, Nano Lett. 10 (2010) 964–973.
[9] X. Lu, M. Mckiernan, Z. Peng, E.P. Lee, H. Yang, Y. Xia, Sci. Adv. Mater. 2 (2010) 413–420.
[10] L. Bu, N. Zhang, S. Guo, X. Zhang, J. Li, J. Yao, T. Wu, G. Lu, J.Y. Ma, D. Su, Science 354 (2016) 1410–1414.
[11] L. Bu, Q. Shao, B. E, J. Guo, J. Yao, X. Huang, J. Am. Chem. Soc. 139 (2017) 9576–9582.
[12] S. Sun, F. Jaouen, J.P. Dodelet, Adv. Mater. 20 (2010) 3900–3904.
[13] S. Sun, G. Zhang, D. Geng, Y. Chen, R. Li, M. Cai, X. Sun, Angew. Chem., Int. Ed. 123 (2011) 442–446.
[14] S. Sun, G. Zhang, Y. Zhong, H. Liu, R. Li, X. Zhou, X. Sun, Chem. Commun. (Camb. 45 (2009) 7048–7050.
[15] Z. Chen, M. Waje, W. Li, Y. Yan, Angew. Chem., Int. Ed. 46 (2007) 4060–4063.
[16] Z. Huang, D. Raciti, S. Yu, L. Zhang, L. Deng, J. He, Y. Liu, N.M. Khashab, C. Wang, J. Gong, J. Am. Chem. Soc. 138 (2016) 6332–6335.

[17] S.M. Alia, G. Zhang, D. Kisailus, D. Li, S. Gu, K. Jensen, Y. Yan, Adv. Funct. Mater. 20 (2010) 3617-3617.
[18] R. Minch, M. Es-Souni, Chem. Commun. 47 (2011) 6284–6286.
[19] J. Lee, J.M. Yoo, Y. Ye, Y. Mun, S. Lee, O.H. Kim, H.W. Rhee, H.I. Lee, Y.E. Sung, J. Lee, Adv. Energy Mater. 5 (2015) 1402093.
[20] L. Su, S. Shrestha, Z. Zhang, W. Mustain, Y. Lei, J. Mater. Chem. A 1 (2013) 12293–12301.
[21] J. Zhu, M. Xiao, X. Zhao, C. Liu, J. Ge, W. Xing, Nano Energy 13 (2015) 318–326.
[22] D.Y. Wang, H.L. Chou, Y.C. Lin, F.J. Lai, C.H. Chen, J.F. Lee, B.J. Hwang, C.C. Chen, Cheminform 43 (2012) 10011–10020.
[23] H. Zhu, S. Zhang, S. Guo, D. Su, S. Sun, J. Am. Chem. Soc. 135 (2013) 7130–7133.
[24] D.R.M. Godoi, J. Perez, H.M. Villullas, J. Phys. Chem. C 113 (2009) 8518–8525.
[25] M. Scofield, C. Koenigsmann, L. Wang, H. Liu, S. Wong, Energy Environ. Sci. 8 (2014) 350–363.
[26] S. Guo, S. Zhang, X. Sun, S. Sun, J. Am. Chem. Soc. 133 (2011) 15354–15357.
[27] Y. Kim, H. Kim, W.B. Kim, Electrochem. Commun. 46 (2014) 36–39.
[28] S.H. Yu, H.H. Li, Q.Q. Fu, L. Xu, S.Y. Ma, Y.R. Zheng, X.J. Liu, Energy Environ. Sci. 10 (2017) 1751–1756.
[29] E. Lebègue, S. Baranton, C. Coutanceau, J. Power Sources 196 (2011) 920–927.
[30] Z. Yan, M. Wang, Y. Lu, R. Liu, J. Zhao, J. Solid State Electrochem. 18 (2014) 1087–1097.
[31] Y. Yin, C.K. Erdonmez, A. Cabot, S. Hughes, A.P. Alivisatos, Adv. Funct. Mater. 16 (2006) 1389–1399.
[32] W. Wang, M. Dahl, Y. Yin, Chem. Mater. 25 (2013) 1179–1189.
[33] Y. Zhao, J. Liu, C. Liu, F. Wang, Y. Song, ACS Catal. 6 (2016) 4127–4134.
[34] L. Xiong, A.M. Kannan, A. Manthiram, Electrochem. Commun. 4 (2002) 898–903.
[35] C.V. Rao, B. Viswanathan, J. Phys. Chem. C 113 (2009) 18907–18913.
[36] W. Ye, S. Chen, M. Ye, C. Ren, J. Ma, R. Long, C. Wang, J. Yang, L. Song, Y. Xiong, Nano Energy 39 (2017) 532–538.
[37] S. Mukerjee, J. Electrochem. Soc. 142 (1995) 1409–1422.
[38] M. Wakisaka, S. Mitsui, Y. Hirose, K. Kawashima, H. Uchida, M. Watanabe, J. Phys. Chem. B 110 (2006) 23489–23496.
[39] G.F. Cabeza, P. Legare, N.J. Castellani, Surf. Sci. 465 (2000) 286–300.
[40] Y. Zhao, Y. Wu, J. Liu, F. Wang, ACS Appl. Mater. Interfaces 9 (2017) 35740–35748.
[41] H. Huang, L. Kan, C. Zhao, L. Luo, Y. Gu, D. Zhang, M. Chao, S. Rui, J. Yang, Z. Peng, J. Zeng, J. Am. Chem. Soc. 139 (2017) 8152–8159.
[42] U.S. Department of Energy, Technical Plan: Fuel Cells, (2016) http://www.energy.gov/sites/prod/files/2016/06/f32/fcto_myrdd_fuel_cells_0.pdf.
[43] S.Y. Ma, H.H. Li, B.C. Hu, C. Xiang, Q.Q. Fu, S.H. Yu, J. Am. Chem. Soc. 139 (2017) 5890–5895.
[44] J. Liu, M. Jiao, L. Lu, H.M. Barkholtz, Y. Li, Y. Wang, L. Jiang, Z. Wu, D.J. Liu, L. Zhuang, Nat. Commun. 8 (2017) 15938.
[45] Y. Wang, K. Yin, J. Zhang, C. Si, X. Chen, L. Lv, W. Ma, H. Gao, Z. Zhang, J. Mater. Chem. A 4 (2016) 14657–14668.
[46] L. Ou, F. Yang, Y. Liu, S. Chen, J. Phys. Chem. C 113 (2009) 20657–20665.
[47] T. Toda, H. Igarashi, H. Uchida, M. Watanabe, J. Electrochem. Soc. 146 (1999) 3750–3756.
[48] W. Chen, J. Kim, S. Sun, S. Chen, J. Phys. Chem. C 112 (2008) 3891–3898.
[49] V.R. Stamenkovic, B.S. Mun, M. Arenz, K.J.J. Mayrhofer, C.A. Lucas, G. Wang, P.N. Ross, N.M. Markovic, Nat. Mater. 6 (2007) 241–247.
[50] M. Oezaslan, F. Hasché, P. Strasser, J. Phys. Chem. Lett. 4 (2013) 3273–3291.
[51] G. Lin, M. Heggen, S. Rudi, P. Strasser, Nano Lett. 12 (2012) 5423–5430.
[52] H. Duan, Q. Hao, C. Xu, J. Power Sources 280 (2015) 483–490.
[53] M. Escudero-Escribano, P. Malacrida, M.H. Hansen, U.G. Vej-Hansen, A. Velázquez-Palenzuela, V. Tripkovic, J. Schiøtz, J. Rossmeisl, I.E. Stephens, I. Chorkendorff, Science 352 (2016) 73.
[54] J.R. Kitchin, J.K. Nørskov, M.A. Barteau, J.G. Chen, J. Chem. Phys. 120 (2004) 10240–10246.